Parabolic Modeling of the Major Temporal Arcade in Retinal Fundus Images

Faraz Oloumi, *Student Member, IEEE*, Rangaraj M. Rangayyan, *Fellow, IEEE*, and Anna L. Ells

Abstract—Monitoring measurements of the openness of the major temporal arcade (MTA) and how they change over time could facilitate improved diagnosis and optimized treatment of retinopathy. We propose methods for the detection, modeling, and measurement of the openness of the MTA, including Gabor filters to detect retinal vessels and the Hough transform to detect and parameterize parabolic forms. Results obtained with 40 images of the Digital Retinal Images for Vessel Extraction database, compared with traces of the MTA drawn by an expert ophthalmologist and a retinal specialist, indicate a low mean distance to the closest point of about 12 pixels (0.24 mm). The proposed methods should facilitate quantitative analysis of the MTA and overcome limitations associated with subjective manual analysis.

Index Terms—Blood vessels, fundus images, Gabor filters, Hough transform, parabolic modeling, retina, retinopathy, temporal arcade.

I. INTRODUCTION

A. Posterior Vascular Changes in the Retina

CHANGES IN the vascular structure of the retina can indicate the presence of several types of pathology, such as hypertension, arteriosclerosis, diabetes, myopia, and retinopathy of prematurity (ROP). The vessels in the retina are modified in terms of their width, shape, and tortuosity by the diseases listed above [1]–[5]. Changes in the architecture of the major temporal arcade (MTA), in the form of a decrease in the angle of insertion of the MTA as well as straightening of the MTA, have been cited as manifestations of at least two types of pathology [1], [5]: as a sequela of ROP and as an indicator of the severity of myopia [1], [5]. The architecture of the MTA is also known to be affected by proliferative diabetic retinopathy due to tractional retinal detachment.

The angle of insertion of the MTA has been loosely defined as the angle between the superior temporal arcade (STA) and the inferior temporal arcade (ITA) as they diverge from the optic nerve head (ONH) and extend toward the periphery of the retina. This angle, also called the arcade angle, is used as an indicator of the structural integrity of the macular region [3], [5]–[7]. Despite the clinical importance of abnormal changes in the architecture of the MTA, only the angle of insertion of the MTA has been quantified in only a few studies: a study dealing with myopia [5] and two studies dealing with ROP [6], [7].

B. Changes in the Angle of Insertion of the MTA

Fledelius and Goldschmidt [5] measured the angle between the STA and the ITA and correlated its decrease to progression of myopia based on follow-up data over a 38-year period. They defined the arcade angle by manually marking cardinal points at the first or the second major arteriole–venule crossings away from the ONH (decided subjectively to represent the direction of the temporal arcade vessels and not just the venule), with the vertex of the angle being at the center of the ONH. The cardinal points were used as landmarks from image to image. Two lines were drawn from the center of the ONH to the marked cardinal points on the ITA and the STA. The angle between the two lines was measured using a transparent angle meter. Fledelius and Goldschmidt [5] reported a decrease of more than $4°$ in the arcade angle in 25% (6 of 24) of the cases with high and stable myopia and in 60% (12 of 20) of the cases with high and progressive myopia. The change in the arcade angle of the progressive myopia group as compared to the stable myopia group was shown to be statistically highly significant $(p < 0.01)$. For the high and progressive myopia group, the change in the arcade angle was shown to be correlated with the degree and increase of myopia.

Change in the angle of insertion of the MTA has also been featured in the classification of retrolental fibroplasia [8] and more recently in the classification of ROP [1]; it has also been used in the evaluation of structural changes following cryotherapy [9]. The Cryotherapy for Retinopathy of Prematurity Cooperative Group [9] evaluated the arcade angle by manually tracking the MTA in $30°$ sectors; however, the normal range of the arcade angle was not defined.

Wilson *et al.* [6] defined the angle of insertion of the MTA as follows: The center of the ONH and the fovea are manually marked by two independent observers. A line is drawn through the manually marked center of the ONH and the fovea; this is the retinal raphe. The image is rotated so that the retinal raphe is horizontal. A line perpendicular to the retinal raphe is drawn from the fovea until it intersects the ITA and the STA. From the intersections, two lines are drawn to the center of the ONH. The total arcade angle (TAA) is defined as the sum of the inferior arcade angle (IAA) and the superior arcade angle
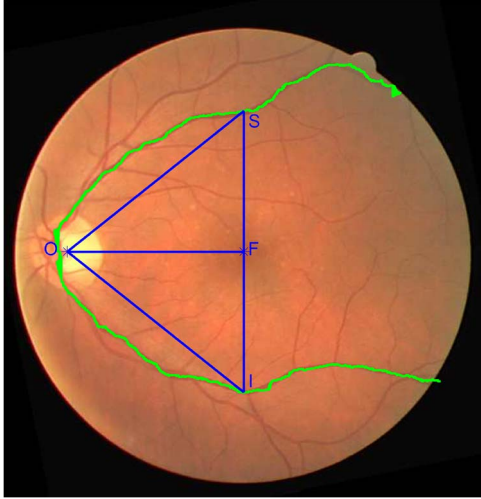
Fig. 1. Image 21 of the DRIVE database illustrating the procedure for measuring the angle of insertion of the MTA as proposed by Wilson *et al.* [2]. The MTA, as traced by a retinal specialist (see Section II-A), is highlighted in green. The points "O" and "F" represent the center of the ONH and the fovea marked by a retinal specialist. The points "S" and "I" represent the intersection of the normal (SI) to the retinal raphe (OF) with the STA and ITA, respectively. The angle $\angle SOF$ is the SAA, the angle $\angle IOF$ is the IAA, and the angle $\angle SOI$ is the TAA. Hence, $TAA = SAA + IAA$, where $SAA = \arctan(SF/OF)$ and $IAA = \arctan(IF/OF)$.

(SAA), as shown in Fig. 1. Wilson *et al.* [6] reported a high degree of interocular symmetry with a mean TAA of 82° for both eyes. They indicated that interocular asymmetry of above 14° to 20° between the two eyes of a patient should be treated with suspicion. A significant level of acuteness in the IAA of the left eye was associated between stages 0 and 1, stages 1 and 2, and stages 1 and 3 of ROP (higher numbers indicate higher severity of ROP).

In a related follow-up study by Wong *et al.* [7], semiautomated measurements were made of four different angles of the temporal and nasal venules and arterioles. The procedures required manual editing of automatically detected vessels; this step required 10–15 min per image. As compared to the previous related study of Wilson *et al.* [6], the angles were measured using reference points selected closer to the center of the ONH. The nasal angles were found to have no statistically significant differences between normal cases and ROP of various stages. The angles of the temporal venules and arterioles were found to have statistically significant differences between normal cases and stage-3 ROP. However, when all stages of ROP were combined, only the angle of the temporal arterioles indicated a statistically significant difference as compared to the normal cases.

By combining a time series of fundus images into short video clips, Ells and MacKeen [10], [11] illustrated that the changes that occur in the MTA in the presence of progressive ROP are dynamic as they alter the posterior architecture of the MTA.

C. Detection of the MTA

Because the MTA originates from the ONH and follows a curved, almost parabolic, path toward the macula, it can be used to detect or estimate the position of the ONH. Furthermore,

relative to the location of the ONH, the macular region can also be estimated or detected [12]–[18].

Foracchia *et al.* [12] proposed a method for the detection of the ONH by defining a directional model for the vessels, assuming that the main vessels originate from the ONH and extend in paths that can be geometrically modeled as parabolas. A directional model was defined using the parabolic formulation and assuming that the preferred direction of the vessels is tangential to the parabolas themselves. With the model and data indicating the center points, direction, and caliber of the vessels, by using a residual sum-of-squares method, the parameters of the model were identified.

Using an estimate of the ONH location and a binarized image of the vasculature, Tobin *et al.* [13] proposed to apply a parabolic model to the statistical distribution of a set of points given by a morphologically skeletonized vascular image to find an estimate of the retinal raphe. A parabola of the form $ay^2 = |x|$ was modified to accommodate for the shifted vertex at the most likely ONH location and the angle of rotation of the retinal raphe β. The resulting model and the skeletonized image were used with a least squares method to estimate the parameters a and β. Even though Tobin *et al.* estimated the openness of the parabolic model, it was only used to draw a parabola on the image.

Using an active shape model and defining a point distribution model, Li and Chutatape [14] proposed a method to detect the boundary of the ONH and the main course of the blood vessels. Using the active shape model and principal component analysis, the location of the ONH was estimated. A modified active shape model was used to extract the main course of the blood vessels. Thirty landmark points on the main course of the vessels were used to derive the point distribution model. The Hough transform and linear least squares fitting methods were combined to estimate a parabolic model.

Fleming *et al.* [15] proposed a method to extract the MTA by means of vessel enhancement and semielliptical curve fitting using the generalized Hough transform (GHT). First, the vessels were enhanced to get a magnitude image and a phase image of the vascular architecture. Assuming that, having an edge map and knowing the orientation of the arcade, a reference point can only be at one of a few locations, the GHT was applied to a skeletonized image of the vasculature. The Hough-space dimension was set to be five, with variables for inclination, horizontal-axis length, left or right opening, and the location of the center of the ellipse. Anatomical restrictions were applied to the variables to limit the number of semiellipses generated by the method. The global maximum in the Hough space was selected as the closest fit to the MTA.

Using steerable filters and color thresholding, Kochner *et al.* [16] extracted edge points on the main blood vessels. An ellipse was then fitted to these points using the GHT. The end of the long axis of the ellipse was taken as an estimate of the location of the ONH.

Ying and Liu [17] obtained a vascular topology map using an energy function defined as the normalized product of the local blood vessel width and density. A quantile threshold was used on the vascular topology map to extract the pixels in a high-energy band. A circle-fitting method was applied to the

extracted pixels to model the MTA as a circle, which was then used to localize the macula.

Niemeijer *et al.* [18] used a point distribution model to represent the ONH, the fovea, and the MTA. The point distribution model consisted of 16 points, where different sets of points were constrained to represent different structures; a set of 10 points was used to mark the MTA. Five hundred retinal images were used to train an optimization algorithm to minimize a cost function and obtain a set of parameters. The cost function employed was based on two global terms, vessel width and orientation, and one local term, structure measurement around the model points. The optimization procedure was performed in both the parameter space and the image space. The set of obtained parameters was used with the same optimization algorithms to minimize the cost function, given an image, to obtain a point distribution model. The methods were tested using another set of 500 images. However, since the MTA model consisted of only ten points, the results of modeling of the MTA were evaluated visually. If all ten points were lying on the correct vessel, as indicated by a human observer, the result was considered to be a complete detection; if only the ITA or the STA was detected, the result was labeled as partial detection. The result was considered to be a failure if neither the former nor the latter was true. Niemeijer *et al.* reported 93.2% complete detection of the MTA, 5.6% partial detection, and 1.2% complete failure to detect the MTA in 500 images of the retina.

The previously published methods to measure the angle of insertion of the MTA, as explained in Section I-B, may not properly reflect the changes that occur in the structure of the MTA, as they only define the openness of the MTA based on three points. Furthermore, only the location of the vertex of the arcade angle has been consistently defined as the center of the ONH; the locations of the other two points have been defined in different manners, as mentioned in Section I-B. Even though the structure of the MTA has been used to estimate the ONH and the macula in previously reported works, only Tobin *et al.* [13] modeled the arcade for parameterization of its openness; however, they used the openness parameter only to draw the parabolic model on the image.

The parabolic or semielliptical profile of the MTA allows for effective modeling using a form of the GHT [19]–[21]. In such a model, changes in the architecture of the MTA could be expected to be reflected as changes in the openness parameter of the parabola: This approach forms the basis for this paper [19]–[21].

II. METHODS

A. Database and Annotation of the MTA

The proposed methods were tested with retinal fundus images from the Digital Retinal Images for Vessel Extraction [22] (DRIVE) database, which contains 40 retinal images of adults. Each image is of size 584×565 pixels, with a field of view (FOV) of $45°$ and a spatial resolution of approximately 20 μm per pixel. The DRIVE database includes 33 images with no abnormal signs and 7 images with signs of diabetic retinopa-

thy, such as exudates, hemorrhages, and pigment epithelium changes. For the purpose of evaluation of the performance of the proposed methods, the STAs and the ITAs in all of the 40 images were traced separately by an expert ophthalmologist and a retinal specialist (A.L. Ells), by magnifying the original image by 145% using the software ImageJ [23]. Only the main venule, the thickest branch, was traced within the FOV. At each branching point, the larger branch was followed. The availability of separate traces of the STA and the ITA facilitates the assessment of the accuracy of the dual-parabolic-modeling procedure as described in Section II-H. The hand-drawn traces of the STA and the ITA can be combined to obtain the trace of the MTA.

The foveae in all of the 40 images were also marked, using the same setup, by the same specialist. The centers of the ONH in all of the images were also marked by A.L. Ells, as described in a related report [24]. The manual markings of the ONH centers and the foveae were used to correct for any rotation existing between the retinal raphe and the horizontal axis of a given image, as described in Section II-G.

B. Overview of the Image Processing Methods

There are three main steps involved in the detection of the MTA.

1) Preprocessing of images [25].
   a) Normalizing each color component in the original image.
   b) Computing the luminance component.
   c) Thresholding the luminance component to obtain the effective area.
   d) Extending the luminance component beyond the effective area to avoid the detection of its edges.
2) Obtaining the skeletons of the MTA, the ITA, and the STA [19], [21] (see Sections II-C and H).
   a) Obtaining the Gabor magnitude response using 180 Gabor filters over the range of $[-90°, 90°]$ to represent the MTA [25].
   b) Separating the Gabor magnitude response image into its superior and inferior parts to represent the STA and the ITA, respectively.
   c) Binarizing the Gabor magnitude response images of the MTA, the ITA, and the STA.
   d) Skeletonizing the binary images.
   e) Applying the morphological process of area open to filter the skeletons.
3) Detecting parabolas and semiparabolas using the GHT [19]–[21] (see Sections II-E and H).
   a) Rotating each skeleton image by $180°$, if the MTA opens to the left (i.e., the image is of the right eye).
   b) Cropping each skeleton image horizontally.
   c) Applying the GHT to the preprocessed skeleton images of the MTA, the STA, and the ITA.
   d) Rotating the Hough space by $180°$, if the MTA opens to the left, and obtaining the parameters of the best-fitting parabolas.

The first step of the proposed algorithm is only presented in point form, because it has been described in detail in one of our

previous publications [25]. The second step is outlined briefly in Section II-C as it has also been presented in detail in our previous related study [19]. The third step is discussed in detail in Section II-E.

C. Detection of the MTA Using Gabor Filters

Gabor filters are sinusoidally modulated Gaussian functions. A Gabor filter is defined by the standard deviation (STD) values of the Gaussian function in the x- and y-directions (σ_x and σ_y) and the frequency f_o of the modulating sinusoid as [25], [26]

$$g(x,y) = \frac{1}{2\pi\sigma_x\sigma_y} \exp\left[-\frac{1}{2}\left(\frac{x^2}{\sigma_x^2} + \frac{y^2}{\sigma_y^2}\right)\right]\cos(2\pi f_o x). \quad (1)$$

To simplify the design procedure, a variable named τ, representing the average thickness of the vessels to be detected, is introduced in the design of the Gabor filter. The value of σ_x is defined in relation to τ as $\sigma_x = \tau/\{2\sqrt{2\ln 2}\}$. The value of f_o is defined as $f_o = 1/\tau$. The parameter σ_y is set as $\sigma_y = 2\sigma_x$. In the present work, we use $\tau = 16$ pixels (0.32 mm).

A set of 180 Gabor filters spanning the range $[-90°, 90°]$ is prepared by rotating the basic Gabor function in (1). A magnitude response image is created by using the maximum value of the responses of the 180 Gabor filters for each pixel. The Gabor magnitude response image is then thresholded at 0.0095 of the normalized intensity to obtain a binarized image. The binarized image is skeletonized [27], and undesired short segments are removed by using the area open procedure [28]. The skeletonization procedure uses the concept of pixel connectedness [29] to delete unwanted pixels and retains lines of single-pixel thickness without altering the structure of the objects. The area open procedure also uses the concept of pixel connectedness [29] to detect segments of connected pixels having less than 70 pixels (as specified in the present work) and removes them.

D. Hough Transform

The Hough transform has long been recognized as a powerful image processing method for the detection of curves, shapes, and motion in images with noisy and irrelevant or even missing data [30], [31]. Hough [32] originally proposed the method for the detection of straight lines in bubble-chamber photographs. The method has since been modified and extended in many different ways, for detection of lines, circles, and parabolic and hyperbolic curves; for estimation of 2-D and 3-D motion; for object recognition; and for detection of arbitrary shapes [30], [31], [33]. The Hough transform refers either to the general process of detection of shapes or to the original method to detect straight lines and its different variations; the GHT refers to all other methods that employ the Hough transform process but detect other shapes and curves instead. Both the Hough transform and the GHT have been used in industrial settings as well as in image processing hardware algorithms for rapid detection of lines and other curves [30]. One of the earliest applications of the GHT in biomedical image processing was demonstrated by Wechsler and Sklansky [34]; they applied the

GHT for the detection of parabolas in X-ray images of the chest to detect the rib cage. Different forms and variations of the GHT have since been used in various biomedical image processing applications [35]–[38].

The Hough transform has several important properties that make it desirable for shape detection and modeling.

1) The Hough transform recognizes partial or slightly misshaped curves and lines, which can pose problems for other shape detection methods.
2) The Hough transform detects shapes in the presence of random and unrelated data.
3) The Hough transform detects several variations of the same shape in the given image in one operation.
4) The Hough transform processes each pixel independently; hence, parallel processing of data is possible for fast hardware implementation.

It should be noted that unwanted data that are similar to the shape to be detected could have an effect on the outcome of the Hough transform and should be treated with care.

The Hough transform reduces a global shape detection problem in the spatial domain to a simpler peak detection problem in a parameter space. Every spatial point that belongs to the pattern leads to a vote on different combinations of parameters that could have caused its presence, if it were part of the shape to be detected. An accumulator matrix is used to store and count the votes; the final count for each accumulator cell indicates the likelihood of the shape, described by the corresponding parameter values of the accumulator cell, belonging to the given pattern in the spatial domain. The size of the accumulator matrix is determined by the number of parameters and their limits.

The Hough transform is said to be similar to template-matching methods, but it is more efficient and advantageous [30], [31], [39]. Template matching is implemented entirely in the spatial domain, whereas the Hough transform is implemented in a parameter domain or the Hough space. In template matching, different templates are generated by shifting and reflecting a basic template and then trying to determine how well the image points match the template points. However, in many instances, corresponding points do not exist in the image domain, which makes the template-matching algorithm inefficient; the Hough transform assumes a match between a given template and an image point and then attempts to determine the transformation parameters that relate the two. The Hough transform does not generate the inessential data that are generated by a template-matching algorithm. Further restrictions on the limits of the Hough-space parameters can make the Hough transform even more efficient.

Specific forms of the Hough transform have also been shown to have similarities to other estimation methods such as the Radon transform and the generalized maximum-likelihood estimators. The Hough transform for line-segment detection has some qualitative properties that are similar to those of the Radon transform. However, the Radon transform cannot provide all of the different variations that are possible to be achieved by the Hough transform [30], [31], [38]. Depending on the kernel function used to relate the image in the spatial

domain to the parameter space, the Hough transform can take on different forms of the class of maximum-likelihood estimators. A quadratic kernel function, for example, implies that the Hough transform could behave like a least squares estimator in the continuous domain; the concept can be extended to the discrete domain [31].

E. GHT for the Detection of Parabolas

Fleming *et al.* [15] and Kochner *et al.* [16] assumed semielliptic and elliptic profiles for the MTA, respectively. However, the MTA diverges away from the ONH toward the macula and then converges down into the macular region. Furthermore, after the second or third branching point, it becomes difficult to distinguish between the original arcade and the new branch as they are both similar in diameter and can branch erratically. The second and third branching points occur approximately over the macula. If one were to use a parametric curve to fit a model to the entire MTA, it would be difficult to define a specific model; an ellipse appears to be the best estimate to the overall vascular structure but not a specific arcade.

The fact that the posterior changes occur close to the ONH, along with *a priori* knowledge of the center of the ONH, and the observation that the macula is situated approximately two ONH diameters (ONHDs) temporal to the ONH [40] are used in the present work to guide the modeling procedure and reduce the computational cost of the algorithm. The average ONHD is about 1.6 mm [40], [41]. The MTA has a parabolic shape up to the macula, so we only need a skeleton of the MTA from the ONH to the macular region for parabolic modeling. There appears to be no useful information on the nasal side of the ONH; thus, this part may also be eliminated. Hence, in the present work, the skeleton image is horizontally limited from $0.25 \times ONHD$ nasal to $2 \times ONHD$ temporal with respect to the center of the ONH. Using the average ONHD and given the spatial resolution of the DRIVE database [22], the width of the image is automatically limited to the range $[O_x - 20, O_x + 160]$, where O_x denotes the x-coordinate of the automatically detected center of the ONH using Gabor filters and phase portrait analysis as described by Rangayyan *et al.* [24].

The general formula defining a parabola with its directrix parallel to the y-axis and its symmetrical axis parallel to the x-axis is

$$(y - y_o)^2 = 4a(x - x_o) \qquad (2)$$

where (x_o, y_o) is the vertex of the parabola and the quantity $4a$ is known as the latus rectum [42]. The absolute value of a defines the aperture or openness of the parabola, and its sign indicates the direction of the opening of the parabola; for a positive a value, the parabola opens to the right [see Fig. 2(a)]. The parameters (x_o, y_o, a) define the parameter domain or the Hough space, represented by an accumulator matrix A. For every nonzero pixel in the image domain, there exists a parabola in the Hough space for each value of a; a single point in the Hough space defines a parabola in the image domain [see Fig. 2(b)–(d)].
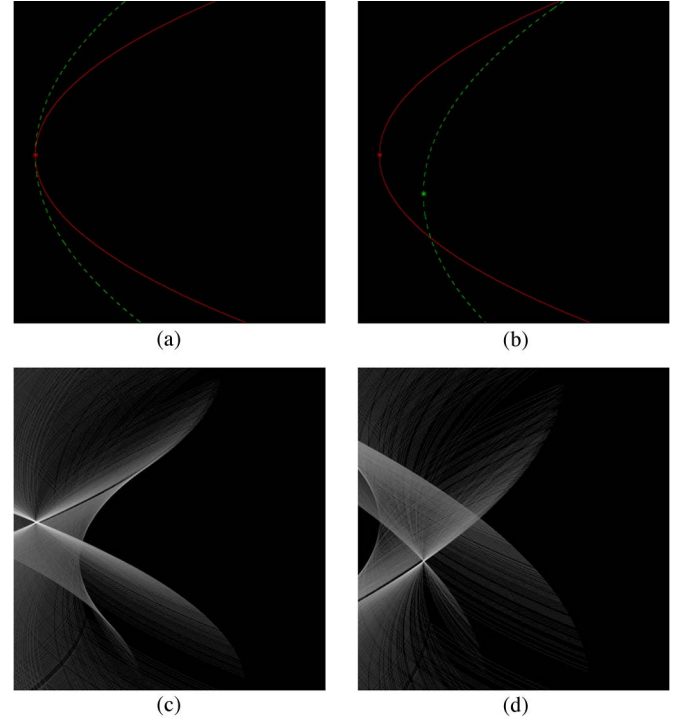

Fig. 2. (a) Test image of size 584 × 565 pixels, showing two parabolas with different openness parameters. The solid red parabola has $a = 60$, and the dashed green one has $a = 120$. Both parabolas share the same vertex for the sake of comparison of their openness. (b) Same parabolas as in (a) but with different vertices. The solid red parabola has its vertex at (40, 280), and the dashed green parabola has its vertex at (120, 350). The top left corner of the image is represented by the coordinates (1, 1). (c) Hough-space plane for $a = 60$ for the image in part (b), showing the detected vertex (41, 280) for the parabola with the smaller aperture as the point with the highest value. (d) Hough-space plane for $a = 120$ for the image in part (b), showing the detected vertex (120, 351) for the parabola with the larger aperture. The detected vertex coordinates, along with the corresponding a value, define the parabolic model.

For the DRIVE images, the size of each (x_o, y_o) plane in the Hough space was defined to be the same as the horizontally cropped skeleton image (584 × 180 pixels). In the present work, the value of a is restricted by physiological limits on the MTA and the size of the image. For the DRIVE database, $|a|$ was confined to the range [35, 120]. In order not to make the accumulator too large, only positive values of a were defined. If an image had the MTA opening to the left (i.e., an image of the right eye), it was rotated by $180°$ so that the MTA would open to the right in the image used for the subsequent steps. Thus, the number of planes in the Hough space for the parameter a was defined to be 86. To make further use of the possible anatomical restrictions, the vertex location (x_o, y_o) of the parabolas represented in the Hough space was restricted to be within $0.25 \times ONHD$ of the automatically detected center of the ONH.

For each nonzero pixel in the given vascular skeleton, the parameter a was computed for each (x_o, y_o) in the Hough space, and the corresponding accumulator cell was incremented by unity if the value of a was within the specified range. Usually, a binarized skeleton image of only the MTA is used in the GHT. However, we can use the Gabor magnitude response of the blood vessels to provide a larger weight to the pixels that

belong to the MTA; the higher the Gabor magnitude response of a pixel, the more likely it belongs to the MTA (for the Gabor parameters used in the present work). Thus, in a variation of the GHT, instead of incrementing each accumulator cell by unity, it was incremented by the Gabor magnitude response of the same pixel. The point in the resulting Hough space with the highest value was selected to obtain the parameters (x_o, y_o, a) of the best-fitting parabolic model to the MTA.

F. Selection of Candidates From the Hough Space

The global maximum in the Hough space may not always present the best-fitting model. Hence, a procedure based on the mean distance to the closest point (DCP) (MDCP) [43] was implemented to select the best fit among the top ten Hough-space candidates. The MDCP measures the closeness of two given contours based on the mean of the DCP from one of the contours (the model) to the other (the reference). Given a model $M = \{m_1, m_2, \ldots, m_N\}$ and a reference $R = \{r_1, r_2, \ldots, r_K\}$, the DCP for a single point m_i on M is defined as

$$DCP(m_i, R) = \min\left(\|m_i - r_j\|\right), \qquad j = 1, 2, \ldots, K \quad (3)$$

where $\|\ \|$ is a norm operator, such as the Euclidean norm. The MDCP is computed as

$$MDCP(M, R) = \frac{1}{N} \sum_{i=1}^{N} DCP(m_i, R). \qquad (4)$$

The smaller the MDCP value is, the closer the fit is to the reference. The MDCP values were calculated for each of the top ten parabolic fits with the automatically detected vascular skeleton serving as the reference. The fit with the smallest MDCP value was selected as the best-fitting model to the MTA. To compare the effects of the vertex restriction and the updating of the accumulator by the Gabor magnitude response, four versions of the GHT were tested: the unity-updated GHT, the unity-updated GHT with the vertex restriction, the Gabor-magnitude-updated GHT, and the Gabor-magnitude-updated GHT with the vertex restriction.

G. Correction of the Retinal Raphe Angle

Any rotation that might exist between the retinal raphe and the horizontal axis of the given image could affect the modeling procedure. The manual markings of the fovea and the center of the ONH were used to determine the rotation angle and correct the image by the same amount. Given (F_x, F_y) and (O_x, O_y) as the coordinates of the fovea and the center of the ONH, respectively, the raphe angle θ is defined as

$$\theta = \arctan\left(\frac{F_y - O_y}{F_x - O_x}\right). \qquad (5)$$

Fig. 3(a) shows an image before and after raphe-angle correction as explained earlier. All of the 40 DRIVE images were rotated, using bilinear interpolation, by their calculated θ values. The same procedures outlined in Section II-B were also
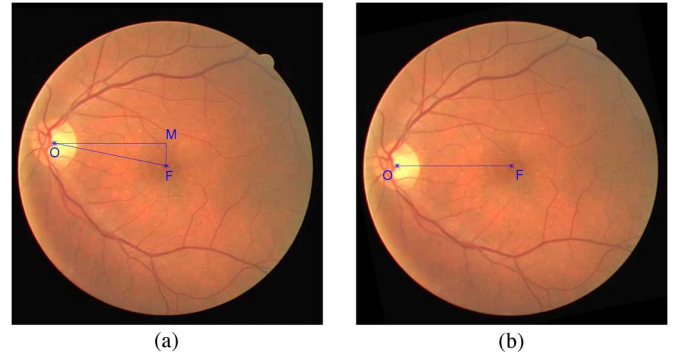

Fig. 3. (a) Image 21 of the DRIVE database (584 × 565 pixels) showing the manually marked fovea (F) and center of the ONH (O). The line OF represents the retinal raphe. The line OM is parallel to the horizontal axis of the image. The retinal raphe angle is defined as $\theta = \arctan(MF/OM)$. (b) Image in (a) with the raphe angle corrected.

applied to all of the 40 DRIVE images with correction for the retinal raphe angles.

H. Dual Parabolic Modeling

The ITA and the STA are often asymmetric; thus, a single parabolic model may match either one of the arcades but not both. Modeling each part of the arcade separately may be a more suitable option. For this purpose, the automatically detected center of the ONH was used to separate the Gabor magnitude response image into its superior and inferior parts. To represent the ITA, any information in the range $y \in [1, O_y]$ was eliminated in the Gabor magnitude response image. Any information within the range $y \in [O_y + 1, 584]$ was eliminated in the Gabor magnitude response image to obtain a representation of the STA. The same procedures as in Section II-C were applied to the superior and inferior Gabor magnitude response images to obtain the vascular skeletons of the STA and ITA, respectively. When modeling each arcade separately, it is essential to restrict the vertex of the resulting parabolas in the Hough space. Otherwise, the procedure will only match a straight segment of the MTA. For this reason, the Gabor-magnitude-updated GHT with the vertex restriction, along with the raphe-angle correction and the MDCP-based selection procedures, was applied to the skeleton images obtained of the STA and the ITA. The part of the fit to the STA in the range $y \in [1, V_y]$ was taken as the STA model, where V_y is the y-coordinate of the detected vertex of the parabola. The ITA model was taken as the fit to the ITA in the range $y \in [V_y, 584]$. This form of modeling results in two openness parameters: a_{STA} and a_{ITA}. Separate analysis of the openness of each arcade (ITA and STA) may be more beneficial as shown by the correlation of the stages of ROP with only the changes in the IAA in the work of Wilson *et al.* [6].

The ITA and the STA converge within the ONH but not necessarily at a single point. Indeed, the arcades drawn by the expert ophthalmologist (A.L. Ells) for the images of the DRIVE database indicate different points of convergence of the ITA and the STA into the ONH. For these reasons, no restriction was placed on the vertices of the two parabolas in the dual-parabolic-modeling procedure other than being located within a

distance of $0.25 \times ONHD$ of the automatically detected center of the ONH.

I. Measures of Performance

In order to evaluate the accuracy of the automatically detected vascular skeleton and the parabolic model derived thereof (*Auto*), as compared to the hand-drawn MTA traces, the unity-updated GHT with the vertex restriction was applied to the hand-drawn traces (*Hand*). The parameters obtained for the hand-drawn traces were compared to the parameters of the parabolic fits from the four GHT versions applied to the vascular skeleton. The Euclidean distance between the two detected vertices, given as

$$d = \sqrt{\left(x_{o_{\text{Hand}}} - x_{o_{\text{Auto}}}\right)^2 + \left(y_{o_{\text{Hand}}} - y_{o_{\text{Auto}}}\right)^2} \quad (6)$$

was used as an error measure for each image. As a second measure, the correlation coefficient r between the two sets of values of the parameter a (for the 40 DRIVE images) was calculated as

$$r = \frac{C(a_{\text{Hand}}, a_{\text{Auto}})}{\sqrt{C(a_{\text{Auto}}, a_{\text{Auto}}) \times C(a_{\text{Hand}}, a_{\text{Hand}})}} \quad (7)$$

where C is the covariance. A correlation coefficient close to unity and a vertex error close to zero would indicate that an accurate vascular skeleton image was obtained over the entire set of images. These measures are used in the present work only to assess the performance of the procedure to derive the vascular skeleton.

To assess the accuracy of the parabolic model for each image, the MDCP was obtained as one measure (see Section II-E). The MDCP was measured from the parabolic model, obtained using each of the variations of the four different GHTs, to the corresponding hand-drawn trace of the MTA, with the latter being treated as the reference. In the case of the dual-parabolic-modeling procedure, the MDCP was measured from the STA and the ITA models to the hand-drawn traces of the STA and the ITA, respectively; hence, two separate measures were obtained for the results of the dual-parabolic-modeling procedure. The lower the MDCP value is, the more accurate the parabolic model is. The MDCP measure was restricted to $2 \times ONHD$ distance from the ONH center (as explained in Section II-E).

The Hausdorff distance [44] was used as another measure to assess the accuracy of the parabolic models. The Hausdorff distance is comparable to the MDCP as it first finds the DCP from each point on the parabolic fit (model) to the corresponding hand-drawn trace (reference) of the MTA. However, instead of taking the mean of all the DCPs, the Hausdorff distance takes their maximum. Given the model $M = \{m_1, m_2, \ldots, m_N\}$ and the reference $R = \{r_1, r_2, \ldots, r_K\}$, the DCP for a single point m_i on M is defined using (3). The Hausdorff distance H from M to R is computed as

$$H(M, R) = \max\{DCP(M, R)\} \quad (8)$$

where $DCP(M, R)$ is an $N \times 1$ vector representing the DCPs for each point on M. It should be noted that the Hausdorff distance is not symmetric, i.e., $H(M, R) \neq H(R, M)$. The
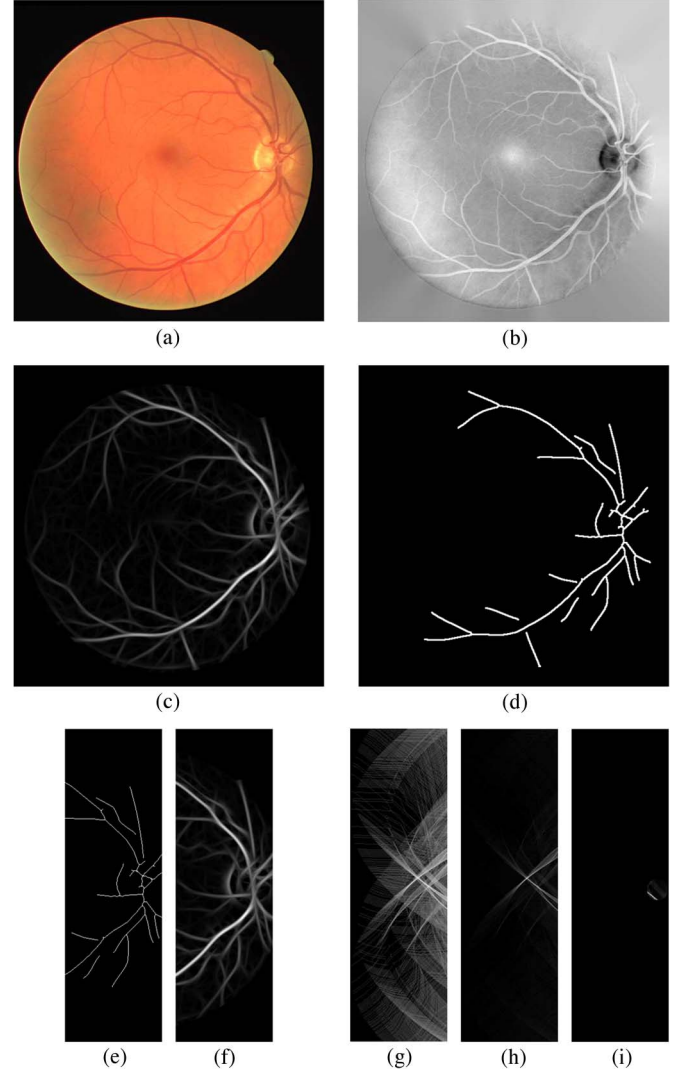

Fig. 4. (a) Image 24 of the DRIVE database (584×565 pixels). (b) Inverted and preprocessed gray-scale image. (c) Gabor magnitude response. (d) Skeletonized and filtered image obtained from the result in (c). (e) Automatically limited skeleton image used in the GHT procedure (584×180 pixels). (f) Automatically limited Gabor magnitude image used to update the Hough space. (g) Hough space for $a = -64$ using the unity-updated GHT without vertex restriction. (h) Hough space for $a = -66$ using the Gabor-magnitude-updated GHT without vertex restriction. (i) Hough space for $a = -75$ using the Gabor-magnitude-updated GHT with vertex restriction.

Hausdorff distance indicates how much the longest distance is from the model to the reference in terms of number of pixels. In the present work, the Hausdorff distance was obtained using the same setup as used to measure the MDCP.

III. RESULTS

The methods were tested using a desktop computer with an Intel Core i7 (hyper-threaded-quad-core) 2.8-GHz processor, an 8-MB level-3 cache, an 8-GB DDR3 RAM, and running 64-b Windows 7 Professional, using a 64-b version of Matlab. The computation time was 27 s to run all of the three steps listed in Section II-B for one image. The original image 24 from the DRIVE database is shown in Fig. 4(a). The inverted and preprocessed gray-scale image used for Gabor filtering is shown in Fig. 4(b). The magnitude response of the Gabor filters

is shown in Fig. 4(c). The thresholded binary image of the blood vessels, which was skeletonized and filtered using the area open procedure, is shown in Fig. 4(d); this result mostly contains the main temporal venule. However, small parts of the main arteriole are also present. The minor vessels are removed by the thresholding step because of their low response due to the large value of the thickness parameter used for the Gabor filters ($\tau = 16$ pixels).

The skeleton and the Gabor magnitude images were automatically clipped horizontally up to the macula, as shown in Fig. 4(e) and (f). The restricted skeleton image was analyzed using the four different variations of the GHT described in Section II-E. The restricted Gabor magnitude image was used in the two Gabor-magnitude-updated versions of the GHT.

The Hough-space plane for $a = -64$ is shown in Fig. 4(g), which contains the global maximum in the case of the unity-updated GHT without the vertex restriction. The Gabor-magnitude-updated GHT had its global maximum in the $a = -66$ plane, as shown in Fig. 4(h). The use of the Gabor magnitude response to update the Hough-space cells increases the intensity for parabolas originating from the thickest branch. Hence, it produces a less crowded Hough space with large values only close to the ONH. For the case of the Gabor-magnitude-updated GHT with the vertex restriction, the global maximum was in the $a = -75$ plane, as shown in Fig. 4(i). The Hough space was only updated if (x_o, y_o), as in (2), was located within a circle with a diameter of $0.5 \times ONHD$ positioned at the automatically detected center of the ONH. This forces a parabolic fit close to the posterior poles.

The hand-drawn trace of the MTA for the image in Fig. 4(a) and its parabolic fit, obtained using the unity-updated GHT with the vertex restriction, are shown in Fig. 5(a). The global maximum was used to determine the three parabolic fits resulting from the unity-updated GHT without vertex restriction, the Gabor-magnitude-updated GHT without vertex restriction, and the Gabor-magnitude-updated GHT with vertex restriction, as shown in Fig. 5(b)–(d), respectively.

The correlation coefficients of the parameter a and the vertex errors of the parabolic fits for the results of the four versions of the GHT, as compared to the parameters of the fits to the corresponding hand-drawn arcades using the unity-updated GHT with vertex restriction, are given in Table I. The Gabor-magnitude-updated GHT with the vertex restriction has led to the highest correlation of the openness parameter a, whereas the unity-updated GHT with the vertex restriction has provided the lowest error in the detected vertices.

Fig. 6(a)–(d) shows the DCP errors for the results of the four GHT versions without raphe-angle correction and MDCP-based selection for image 2 of the DRIVE database. The DCP, from the parabolic model to the hand-drawn MTA, is drawn in the illustrations only for every fifth point on the model. Fig. 6(e) shows the DCP errors for the result of the Gabor-magnitude-updated GHT with vertex restriction and raphe-angle correction. The DCP for the Gabor-magnitude-updated GHT with vertex restriction, raphe-angle correction, and MDCP-based selection is shown in Fig. 6(f). The lower MDCP errors for the results in Fig. 6(e) and (f) as compared to the result in Fig. 6(d) are apparent by visual inspection.
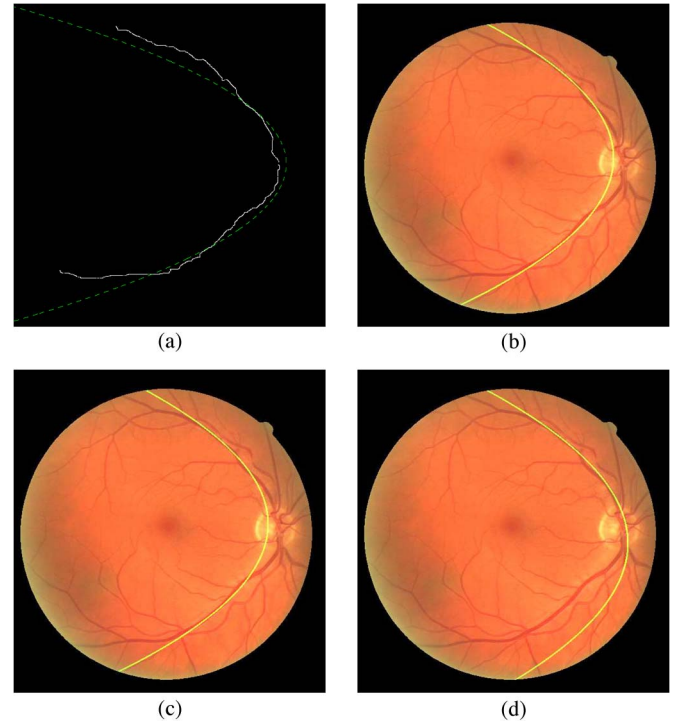

Fig. 5. All of the parabolic fits shown in this figure were obtained by taking the global maximum in their corresponding Hough spaces. (a) Hand-drawn trace of the MTA for the image in Fig. 4(a) and (dashed green curve) its parabolic fit obtained using the unity-updated GHT with vertex restriction. The parameters of the parabola are (494, 291, −41). (b) Best-fitting parabola obtained from the unity-updated GHT without vertex restriction, with the parameters (463, 279, −64). (c) Best-fitting parabola obtained from the Gabor-magnitude-updated GHT without vertex restriction; the parameters are (460, 279, −66). (d) Best-fitting parabola obtained from the Gabor-magnitude-updated GHT with vertex restriction, having the parameters (489, 314, −75). Although the models in (b) and (c) may appear to be similar, the detected vertices and the a parameters are different.

Fig. 7(a) shows an example of modeling the ITA and STA separately: The cyan semiparabola is the fit to the STA, and the dark blue semiparabola is the fit to the ITA; the models do not share the same vertex and have different a parameters. Fig. 7(e) shows the DCP errors for the ITA model as compared to the hand-drawn trace of the ITA. Similarly, Fig. 7(f) shows the DCP errors for the STA model as compared to the hand-drawn trace of the STA. By comparing Fig. 7(e) and (f) to Fig. 7(b)–(d), it is obvious that the dual-parabolic-modeling procedure produces more accurate fits than the single-parabolic-modeling procedure. Fig. 8 shows the DCP errors for the results of dual parabolic modeling for image 19 of the DRIVE database; for the sake of comparison of the ITA and the STA fits, both models are combined in one image. It can be observed that the STA has a semiparabolic shape, whereas the ITA resembles an exponential curve; this point is reinforced by the low MDCP for the STA model as compared to the above-average MDCP for the ITA model.

The average MDCP and Hausdorff distances of the parabolic fits for the results of the four different versions of the GHT and the dual-parabolic-modeling procedure, as compared to the hand-drawn arcades for all of the 40 DRIVE images, are listed in Tables II and III, respectively. Both of the measures were also used to assess the performance of the modeling methods with

TABLE I
CORRELATION COEFFICIENTS AND AVERAGE VERTEX ERRORS BETWEEN THE PARAMETERS OF THE PARABOLAS OBTAINED
WITH THE FOUR DIFFERENT GHT VERSIONS COMPARED TO THE PARAMETERS OF THE UNITY-UPDATED GHT
APPLIED TO THE HAND-DRAWN ARCADES FOR ALL 40 DRIVE IMAGES. THE AVERAGE VERTEX ERRORS
AND THEIR STDS ARE IN TERMS OF PIXELS, WHERE EACH PIXEL IS APPROXIMATELY 20 μm

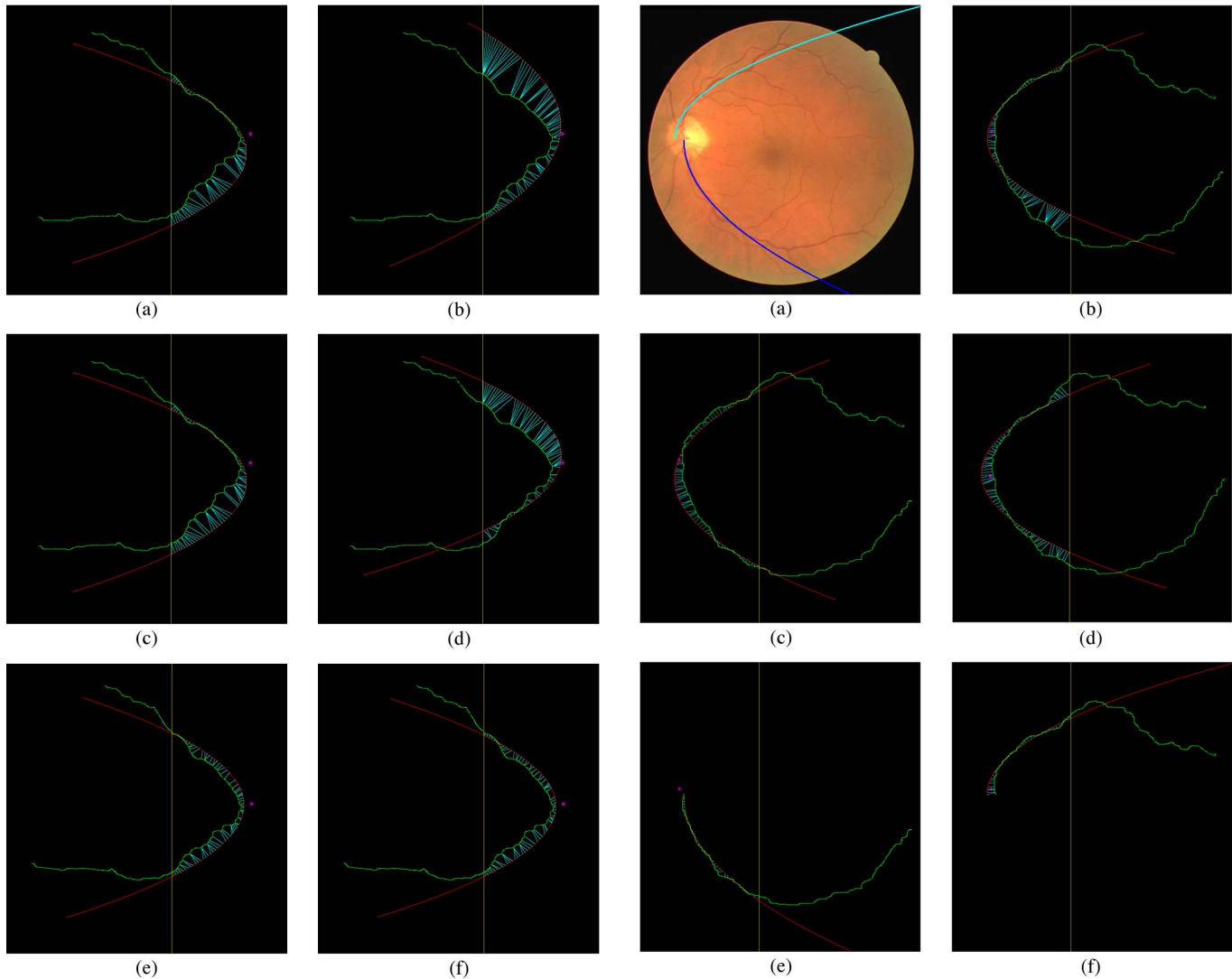| GHT Version	Correlation Coefficient	Vertex Error, Mean $\pm$ STD (Pixels)
Unity-updated	0.91	37.65 ± 35.17
Unity-updated with Vertex Restriction	0.96	10.61 ± 8.18
Gabor-magnitude-updated	0.92	36.82 ± 25.18
Gabor-magnitude-updated with Vertex Restriction	0.97	12.53 ± 9.2

Fig. 6. In each case, the red line represents the parabolic model, and the green trace represents the hand-drawn arcade for image 2 of the DRIVE database. The magenta asterisk indicates the automatically detected center of the ONH. The yellow vertical line shows the automatically determined horizontal extent of MDCP measurement from the ONH. The cyan lines connecting the model to the hand-drawn arcade are the DCPs. Neither raphe-angle correction nor MDCP-based selection was applied in cases (a)–(d). (a) MDCP for the unity-updated GHT is 17.63 pixels (0.35 mm). (b) MDCP for the unity-updated GHT with vertex restriction is 38.19 pixels (0.76 mm). (c) MDCP for the Gabor-magnitude-updated GHT is 17.63 pixels (0.35 mm). (d) MDCP for the Gabor-magnitude-updated GHT with vertex restriction is 25.04 pixels (0.5 mm). (e) MDCP for the Gabor-magnitude-updated GHT with vertex restriction and raphe-angle correction is 12.63 pixels (0.25 mm). (f) MDCP for the Gabor-magnitude-updated GHT with vertex restriction, raphe-angle correction, and MDCP-based selection is 12.33 pixels (0.24 mm).
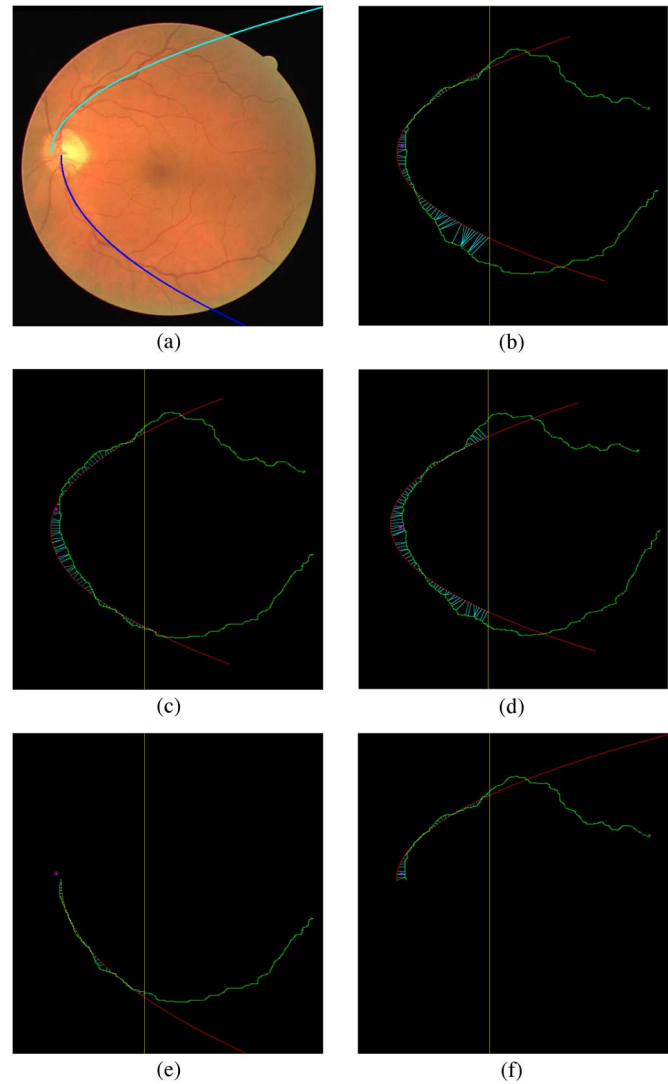
Fig. 7. Example of the dual-parabolic-modeling procedure with image 9 of the DRIVE database. Each arcade (ITA and STA) is modeled separately. (a) (Cyan) STA and (dark blue) ITA models obtained with the Gabor-magnitude-updated GHT with vertex restriction. (b) MDCP for a single parabolic model obtained using the Gabor-magnitude-updated GHT with vertex restriction is 12.22 pixels (0.24 mm). (c) MDCP for a single parabolic model obtained using the Gabor-magnitude-updated GHT with vertex restriction and raphe-angle correction is 8.61 pixels (0.17 mm). (d) MDCP for a single parabolic model obtained using the Gabor-magnitude-updated GHT with vertex restriction, raphe-angle correction, and MDCP-based selection is 11.50 pixels (0.23 mm). (e) MDCP for the ITA model in (a) is 2.16 pixels (0.04 mm). (f) MDCP for the STA model in (a) is 4.26 pixels (0.08 mm).
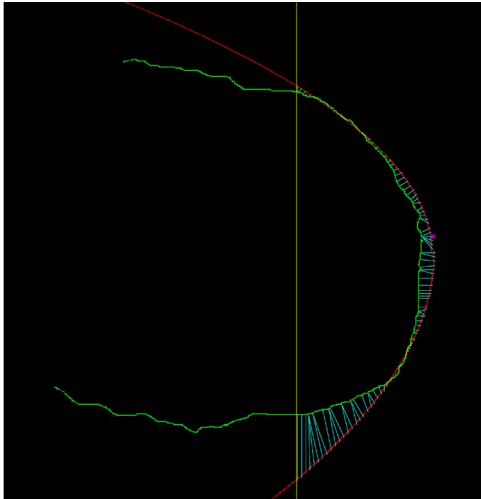
Fig. 8. Illustration of the DCPs for the result of dual parabolic modeling for image 19 of the DRIVE database using the Gabor-magnitude-updated GHT with vertex restriction. The MDCP for the STA model is 5.53 pixels (0.11 mm). The MDCP for the ITA model is 20.58 pixels (0.41 mm).

the added procedures of raphe-angle correction and MDCP-based selection, separately and combined together. The dual-parabolic-modeling procedure provides separate models for the ITA and the STA; hence, the MDCP and the Hausdorff measures were obtained for each of the ITA and STA models separately as compared to their corresponding hand-drawn traces. Combining the ITA and the STA models to obtain the MDCP and the Hausdorff measures, for the sake of comparison to the results of the other GHT versions, is not appropriate as it may bias the final results. Therefore, direct comparison of the results of single parabolic modeling to the results of dual parabolic modeling may not be meaningful in the case of MDCP. However, since the Hausdorff distance is an indicator of the possibility of getting large distances on the average, a direct comparison of the Hausdorff distances for the results of the dual-parabolic-modeling procedure to the Hausdorff distances for the results of the single-parabolic-modeling procedure is acceptable.

Among the four different versions of the GHT for single parabolic modeling (see Table II), the two Gabor-magnitude-updated procedures have lower MDCP, on the average, with and without the raphe-angle correction and the MDCP-based selection being used, as compared to the unity-updated GHT procedures. The results of the dual-parabolic-modeling procedure for the STA have a higher MDCP, on the average, as compared to the results of modeling of the ITA, which can be partly attributed to the high MDCP produced by several oddly shaped STAs in the DRIVE images, also evident from the high STD in the MDCP of the STA models. The added procedures of raphe-angle correction and MDCP-based selection have less impact when used separately; combining the two appears to have a bigger influence on the results of the unity-updated GHTs as compared to the Gabor-magnitude-updated GHTs. The raphe-angle correction and MDCP-based selection methods have a minor effect when applied to the dual-parabolic-modeling procedure as compared to the single-parabolic-modeling procedures. The Hausdorff distances (see

Table III) indicate that the dual-parabolic-modeling procedure produces lower errors, on the average, for both the ITA and the STA models as compared to all four of the single-parabolic-modeling procedures.

In order to test the statistical significance of the differences in the MDCP of the results provided by the various modeling options, the p-values for many selected pairs of sets of MDCP values were computed. The differences between the MDCPs obtained using raphe-angle correction by itself, as compared to the single-parabolic-modeling procedures without any options, have no statistical significance; the same is true when only using the MDCP-based selection option. When both raphe-angle correction and MDCP-based selection are combined, only the difference between the MDCPs for the Gabor-magnitude-updated GHT with vertex restriction with and without both options is statistically significant ($p = 0.0252$).

In the case of dual parabolic modeling, the differences between the MDCPs with and without raphe-angle correction and MDCP-based selection (separately and combined) were found to have no statistical significance. The difference between the MDCPs of dual parabolic modeling with MDCP-based selection and single parabolic modeling using the unity-updated GHT is statistically significant with $p = 0.0242$.

The differences between the MDCPs of a few other pairs of options, such as the unity-updated GHT as compared with the Gabor-magnitude-updated GHT (without any other option), the Gabor-magnitude-updated GHT with and without vertex restriction, and the Gabor-magnitude-updated GHT with and without all of the options listed in Table II, were found to have no statistical significance.

IV. DISCUSSION

In comparison with our pilot and preliminary studies [19]–[21], the addition of the anatomical restrictions on the vessel map and the search area in the Hough space, as well as the use of Gabor-magnitude-weighted increments, has significantly improved the results. By limiting the search area for the vertex to be close to the automatically detected center of the ONH, the Hough procedure is forced to fit the parabolic model to the posterior part of the MTA. By restricting the vessel map up to the macula, the parabolic profile of the appropriate portion of the MTA is emphasized. Updating the Hough space with the Gabor magnitude response reduces the influence of smaller vessels on the result. This is also confirmed by the lower average MDCP values for the results of the Gabor-magnitude-updated GHTs as compared to those of the unity-updated GHTs (see Tables II and III).

The high correlation between the values of the parameter a obtained automatically and from the hand-drawn MTAs indicates that the automatically obtained vessel skeleton maps are accurate.

The MDCP-based selection procedure, applied to the raphe-angle-corrected images, helps to improve the accuracy of the models. The addition of the raphe-angle correction and the MDCP-based selection procedures to the single-parabolic-modeling GHTs appears to have the same impact as the dual-parabolic-modeling procedure without the use of raphe-angle

TABLE II
AVERAGE MDCP (IN PIXELS, WHERE EACH PIXEL IS APPROXIMATELY 20 μm) OF THE PARABOLIC FITS FOR THE FOUR VERSIONS OF THE GHT AND THE DUAL-PARABOLIC-MODELING PROCEDURE, AS COMPARED TO THE HAND-DRAWN MTAs FOR ALL 40 DRIVE IMAGES. THE MDCP VALUES FOR THE PROCEDURES WITH RAPHE-ANGLE CORRECTION, MDCP-BASED SELECTION IN THE HOUGH SPACE, AND BOTH COMBINED ARE ALSO PROVIDED

GHT Version	MDCP, Mean $\pm$ STD	With raphe-angle correction	With MDCP-based selection	With raphe-angle correction and MDCP-based selection
Unity-updated	18.35 ± 11.40	16.62 ± 9.42	16.26 ± 9.93	14.20 ± 7.07
Unity-updated with Vertex Restriction	16.27 ± 8.84	15.09 ± 7.85	15.15 ± 8.13	13.45 ± 7.54
Gabor-magnitude-updated	14.08 ± 9.93	13.93 ± 9.20	12.68 ± 8.80	12.79 ± 8.63
Gabor-magnitude-updated with Vertex Restriction	16.06 ± 9.05	12.64 ± 6.39	14.59 ± 8.00	12.10 ± 6.16
Gabor-magnitude-updated with Vertex Restriction, ITA Model	12.07 ± 8.88	12.33 ± 11.02	10.90 ± 8.71	10.64 ± 8.76
Gabor-magnitude-updated with Vertex Restriction, STA Model	15.01 ± 16.32	14.09 ± 15.28	14.52 ± 16.71	13.93 ± 16.06

TABLE III
AVERAGE HAUSDORFF DISTANCE (IN PIXELS, WHERE EACH PIXEL IS APPROXIMATELY 20 μm) OF THE PARABOLIC FITS FOR THE FOUR VERSIONS OF THE GHT AND THE DUAL-PARABOLIC-MODELING PROCEDURE, AS COMPARED TO THE HAND-DRAWN MTAs FOR ALL 40 DRIVE IMAGES. THE HAUSDORFF DISTANCE VALUES FOR THE PROCEDURES WITH RAPHE-ANGLE CORRECTION, MDCP-BASED SELECTION, AND BOTH COMBINED ARE ALSO PROVIDED

GHT Version	Hausdorff, Mean $\pm$ STD	With raphe-angle correction	With MDCP-based selection	With raphe-angle correction and MDCP-based selection
Unity-updated	53.14 ± 34.42	49.17 ± 31.10	50.17 ± 34.27	42.50 ± 24.82
Unity-updated with Vertex Restriction	45.49 ± 22.33	40.94 ± 18.61	43.12 ± 20.78	36.75 ± 17.70
Gabor-magnitude-updated	45.82 ± 34.52	46.05 ± 32.50	42.32 ± 29.29	43.55 ± 33.62
Gabor-magnitude-updated with Vertex Restriction	46.72 ± 26.49	36.28 ± 15.63	42.51 ± 21.60	34.90 ± 16.60
Gabor-magnitude-updated with Vertex Restriction, ITA Model	34.19 ± 15.70	35.25 ± 20.46	30.18 ± 15.73	29.80 ± 16.46
Gabor-magnitude-updated with Vertex Restriction, STA Model	39.66 ± 31.51	38.06 ± 30.25	37.38 ± 32.27	36.36 ± 31.29

correction and MDCP-based selection. The addition of the raphe-angle correction and the MDCP-based selection options makes no statistically significant improvement over the results of the dual-parabolic-modeling procedure. The dual-parabolic-modeling procedures are more reliable as they are less likely to result in a large error as shown by the lower Hausdorff distances, on the average, as compared to the single-parabolic-modeling procedures.

Although the results obtained are encouraging, there are still limitations that need to be addressed. If the major arteriole arcade is adequately thick, it may not get eliminated in the binarization step and could affect the modeling procedure. A method to distinguish between venules and arterioles could be used to eliminate the arterioles [45], [46].

As mentioned in Section II-C, in the present work, a bank of 180 Gabor filters is used to detect the MTA; the number of filters used can be reduced by considering the orientation range of the MTA, the computational cost, and the required detection accuracy [47].

The present work is concerned with quantitative representation of the architecture of the MTA; the previously published modeling methods (see Section I-C) have not modeled the MTA for quantitative analysis of its architecture. Even though the GHT has many similarities with other modeling methods (see Section II-D), a comparison of the single-parabolic-modeling procedure with the modeling methods mentioned in Section I-C (in terms of accuracy and execution time) could be beneficial as a separate study, as all of the mentioned methods will have to be implemented first and then tested with the current experimental setup. However, such a comparison with the dual-parabolic-modeling procedure is not feasible.

The raphe angles of the 40 images of the DRIVE database have an average of approximately $6°$. Hence, in the present work, manual markings of the foveae and the ONH centers were used to obtain precise measurements of the raphe angles and to demonstrate the effects of raphe-angle correction on the modeling procedures. An automated method [13], [14], [17] may be used to detect the fovea, and the results could be used along with the automatically detected center of the ONH [24] to correct for raphe-angle rotation. However, as indicated in the preceding discussion in Section III, using the raphe-angle correction option makes no statistically significant difference in the results of the single- and dual-parabolic-modeling procedures (for the DRIVE images). Hence, manual marking or automatic detection of the fovea is not essential for modeling of the MTA if the variations in the raphe angle are comparable to those found in the DRIVE images.

Retinal fundus images of preterm infants typically lack a clear depiction of the fovea; as shown by Chiang *et al.* [48], there is significant variability between ROP experts in the identification of the fovea in wide-angle retinal images of preterm infants at risk of ROP. This fact may preclude the application of the method of Wilson *et al.* [2] for the measurement of the arcade angle, which is dependent on the location of the fovea. The methods proposed in the present work require only the location of the ONH (for which we have already proposed an automatic method [24]) and provide the advantage of requiring a single landmark.

The proposed methods were tested on the DRIVE images in the present work; however, the DRIVE database neither has information regarding the arcade angle nor does contain information regarding possible diseases that affect the architecture of the MTA. Regardless, it is one of the few public databases that are commonly used in the design and evaluation of algorithms for the analysis of retinal images. The DRIVE database has served the main purpose of the present work, which is to develop image processing methods for the detection and modeling of the MTA as well as their assessment using a well-established database of retinal images.

The accuracy of the procedure for the detection of the MTA can be affected by the presence of lesions and other abnormal features. Even though the DRIVE database includes cases with signs of diabetic retinopathy in the form of lesions and hemorrhages, the proposed methods should be tested with a different database of retinal fundus images to further assess their accuracy and robustness; this is a work in progress.

The present work is concerned with modeling and parametric representation of the MTA. The nasal arcade has a shorter distance to the ora serrata than the MTA and, hence, is less vulnerable to distortion. Furthermore, as shown by Wong *et al.* [7], the changes in the nasal arcade angles have no statistical significance in the presence of ROP.

Possible changes in the thickness and tortuosity of retinal blood vessels that are expected to occur in the presence of ROP have been found to be not consistently correlated to the stages of ROP [2], [49], [50]. Moreover, detection accuracy of changes in the thickness and tortuosity of the blood vessels can be affected by low quality and presence of artifacts in images of preterm infants [7]. Detection and analysis of architectural parameters of the MTA, as proposed in the present work, could improve the diagnosis, staging, decision making for surgical treatment, and clinical management of ROP.

Parabolic modeling, as proposed in the present work, characterizes the architecture of the MTA up to the macular region, whereas the procedure of Wilson *et al.* [2] quantifies an angle based on the location of the ONH and two specific points on the ITA and STA that reflect the location of the fovea (see Fig. 1). This observation implies that the two measures are fundamentally different from one another; this point was confirmed by low correlations (0.65, 0.63, and 0.42) between the automatically measured values of the TAA, the IAA, and the SAA using the procedure described by Wilson *et al.* [2] and the automatically obtained openness parameters a_{MTA}, a_{ITA}, and a_{STA}, respectively. As shown by Ells and MacKeen [10], [11], analyzing the overall architecture of the MTA is more desirable than analyzing the variations in the angle of insertion of the MTA in the presence of progressive ROP.

Retinal fundus images of pediatric cases differ from those of adult cases in color and relative size of the features, which are mainly the blood vessels. Detection and analysis of the openness of the MTA in fundus images of preterm infants should be possible by fine tuning the parameters of the Gabor filters and the GHT procedures. There is no publicly available annotated database of retinal images related to ROP. Application of the methods proposed in the present work to a database of fundus images of cases of ROP [51] is planned after the database is annotated with clinical interpretation in terms of stages of ROP and hand-drawn traces of the MTA.

Even though the dual-parabolic-modeling approach improves the results, it can still be biased if the ITA or the STA has nonlinear rates of divergence (see Fig. 8). A parabola has a linear divergence rate controlled by the parameter a. An exponential model, however, can have different divergence rates dictated by its power. Hence, modeling each arcade separately using an exponential model may be more suitable and will be explored in future studies.

V. CONCLUSION

We have proposed parabolic modeling methods using the GHT to detect, measure, and parameterize the architecture of the MTA in retinal fundus images. The two anatomical restrictions imposed on the width of the image as well as the search area for the vertex of the parabolic model have improved the performance of the modeling procedure. The global maximum in the Hough space does not always provide the best-fitting model, as shown by the improved results of modeling by using MDCP-based selection in the Hough space. Correction of the retinal raphe angle provides no statistically significant difference in the results of the single- and dual-parabolic-modeling procedures (with the DRIVE database). The fact that the fully automatic dual-parabolic-modeling procedure provides the highest improvement in the modeling results makes it the most significant option among the modeling procedures presented. Exponential models fitted to the STA and the ITA separately should provide more accurate models. We propose to test the methods on a time series of fundus images of preterm infants and correlate the changes in the model parameters to the different stages of ROP.

REFERENCES

[1] "The international classification of retinopathy of prematurity revisited," *Arch. Ophthalmol.*, vol. 123, no. 7, pp. 991–999, Jul. 2005.

[2] C. M. Wilson, K. D. Cocker, M. J. Moseley, C. Paterson, S. T. Clay, W. E. Schulenburg, M. D. Mills, A. L. Ells, K. H. Parker, G. E. Quinn, A. R. Fielder, and J. Ng, "Computerized analysis of retinal vessel width and tortuosity in premature infants," *Invest. Ophthalmol. Vis. Sci.*, vol. 49, no. 8, pp. 3577–3585, Aug. 2008.

[3] H. F. Jelinek and M. J. Cree, "Introduction," in *Automated Image Detection Retinal Pathology*, H. F. Jelinek and M. J. Cree, Eds. Boca Raton, FL: CRC Press, 2010.

[4] N. Patton, T. M. Aslam, T. MacGillivray, I. J. Deary, B. Dhillon, R. H. Eikelboom, K. Yogesan, and I. J. Constable, "Retinal image analysis: Concepts, applications and potential," *Progr. Retinal Eye Res.*, vol. 25, no. 1, pp. 99–127, Jan. 2006.

[5] H. C. Fledelius and E. Goldschmidt, "Optic disc appearance and retinal temporal vessel arcade geometry in high myopia, as based on follow-up data over 38 years," *Acta Ophthalmol.*, vol. 88, no. 5, pp. 514–520, Aug. 2010.

[6] C. Wilson, M. Theodorou, K. D. Cocker, and A. R. Fielder, "The temporal retinal vessel angle and infants born preterm," *Brit. J. Ophthalmol.*, vol. 90, no. 6, pp. 702–704, Jun. 2006.

[7] K. Wong, J. Ng, A. L. Ells, A. R. Fielder, and C. M. Wilson, "The temporal and nasal retinal arteriolar and venular angles in preterm infants," *Brit. J. Ophthalmol.*, vol. 95, no. 12, pp. 1723–1727, Dec. 2011.

[8] A. B. Reese, M. J. King, and W. C. Owens, "A classification of retrolental fibroplasia," *Amer. J. Ophthalmol.*, vol. 36, no. 10, pp. 1333–1335, Oct. 1953.

[9] "Multicenter trial of cryotherapy for retinopathy of prematurity: Ophthalmological outcomes at 10 years," *Arch. Ophthalmol.*, vol. 119, no. 8, pp. 1110–1118, Aug. 2001.

[10] A. L. Ells and L. D. MacKeen, "Retinopathy of prematurity—The movie," *J. Amer. Assoc. Pediatr. Ophthalmol. Strabismus*, vol. 8, no. 4, p. 389, Aug. 2004.

[11] A. L. Ells and L. D. MacKeen, "Dynamic documentation of the evolution of retinopathy of prematurity in video format," *J. Amer. Assoc. Pediatr. Ophthalmol. Strabismus*, vol. 12, no. 4, pp. 349–351, Aug. 2008.

[12] M. Foracchia, E. Grisan, and A. Ruggeri, "Detection of optic disc in retinal images by means of a geometrical model of vessel structure," *IEEE Trans. Med. Imag.*, vol. 23, no. 10, pp. 1189–1195, Oct. 2004.

[13] K. W. Tobin, E. Chaum, V. P. Govindasamy, and T. P. Karnowski, "Detection of anatomic structures in human retinal imagery," *IEEE Trans. Med. Imag.*, vol. 26, no. 12, pp. 1729–1739, Dec. 2007.

[14] H. Li and O. Chutatape, "Automated feature extraction in color retinal images by a model based approach," *IEEE Trans. Biomed. Eng.*, vol. 51, no. 2, pp. 246–254, Feb. 2004.

[15] A. D. Fleming, K. A. Goatman, S. Philip, J. A. Olson, and P. F. Sharp, "Automatic detection of retinal anatomy to assist diabetic retinopathy screening," *Phys. Med. Biol.*, vol. 52, no. 2, pp. 331–345, Jan. 2007.

[16] B. Kochner, D. Schuhmann, M. Michaelis, G. Mann, and K. H. Englmeier, "Course tracking and contour extraction of retinal vessels from color fundus photographs: Most efficient use of steerable filters for model based image analysis," in *Proc. SPIE Med. Imag.*, San Diego, CA, Feb. 1998, vol. 3338, pp. 755–761.

[17] H. Ying and J. C. Liu, "Automated localization of macula–fovea area on retina images using blood vessel network topology," in *Proc. IEEE Int. Acoust., Speech, Signal Process. Conf.*, Mar. 2010, pp. 650–653.

[18] M. Niemeijer, M. D. Abràmoff, and B. van Ginneken, "Segmentation of the optic disk, macula and vascular arch in fundus photographs," *IEEE Trans. Med. Imag.*, vol. 26, no. 1, pp. 116–127, Jan. 2007.

[19] F. Oloumi and R. M. Rangayyan, "Detection of the temporal arcade in fundus images of the retina using the Hough transform," in *Proc. 31st IEEE Annu. Int. Eng. Med. Biol. Soc. Conf.*, Minneapolis, MN, Sep. 2009, pp. 3585–3588.

[20] F. Oloumi, R. M. Rangayyan, and A. L. Ells, "Parametric representation of the retinal temporal arcade," in *Proc. 10th IEEE ITAB*, Corfu, Greece, Nov. 2010, pp. 1–4, [CD-ROM].

[21] F. Oloumi, R. M. Rangayyan, and A. L. Ells, "Dual-parabolic modeling of the superior and the inferior temporal arcades in fundus images of the retina," in *Proc. IEEE MeMeA*, Bari, Italy, Jun. 2011, pp. 1–6.

[22] DRIVE: Digital Retinal Images for Vessel Extraction. [Online]. Available: www.isi.uu.nl/Research/Databases/DRIVE/download.php, last accessed on Jun. 21, 2011

[23] Image Processing and Analysis in Java. [Online]. Available: http://rsbweb.nih.gov/ij/, accessed on Sep. 3, 2008

[24] R. M. Rangayyan, X. Zhu, F. J. Ayres, and A. L. Ells, "Detection of the optic nerve head in fundus images of the retina with Gabor filters and phase portrait analysis," *J. Digit. Imag.*, vol. 23, no. 4, pp. 438–453, Aug. 2010.

[25] R. M. Rangayyan, F. J. Ayres, O. Faraz, O. Foad, and P. Eshghzadeh-Zanjani, "Detection of blood vessels in the retina with multiscale Gabor filters," *J. Electron. Imag.*, vol. 17, no. 2, pp. 023018-1–023018-7, Apr.–Jun. 2008.

[26] F. J. Ayres and R. M. Rangayyan, "Design and performance analysis of oriented feature detectors," *J. Electron. Imag.*, vol. 16, no. 2, pp. 023007-1–023007-12, Apr.–Jun. 2007.

[27] C. Arcelli and G. Sanniti di Baja, "Skeletons of planar patterns," in *Topological Algorithms for Digital Image Processing*, vol. 19, *Machine Intelligence and Pattern Recognition*, T. Y. Kong and A. Rosenfeld, Eds. Amsterdam, The Netherlands: North-Holland, 1996, pp. 99–143.

[28] S. T. Acton, "A pyramidal algorithm for area morphology," in *Proc. IEEE Int. Conf. Image Process.*, Vancouver, BC, Canada, Sep. 2000, pp. 954–957.

[29] T. Y. Kong and A. Rosenfeld, "Digital topology: Introduction and survey," *Comput. Vis., Graph., Image Process.*, vol. 48, no. 3, pp. 357–393, Dec. 1989.

[30] J. Illingworth and J. Kittler, "A survey of the Hough transform," *Comput. Vis., Graph., Image Process.*, vol. 44, no. 1, pp. 87–116, Oct. 1988.

[31] J. Princen, J. Illingworh, and J. Kittler, "A formal definition of the Hough transform: Properties and relationships," *J. Math. Imag. Vis.*, vol. 1, no. 2, pp. 153–168, Jul. 1992.

[32] P. V. C. Hough, "Method and Means for Recognizing Complex Patterns," U.S. Patent 3 069 654, Dec. 18, 1962.

[33] M. Z. M. Jafri and F. Deravi, "Efficient algorithm for the detection of parabolic curves," in *Proc. SPIE Vis. Geometry III*, 1995, vol. 2356, no. 1, pp. 53–62.

[34] H. Wechsler and J. Sklansky, "Finding the rib cage in chest radiographs," *Pattern Recognit.*, vol. 9, no. 1, pp. 21–30, Jan. 1977.

[35] W. Lu, "Hough Transforms for Shape Identification and Applications in Medical Image Processing," Ph.D. thesis, Univ. Missouri, Columbia, MO, 2003.

[36] K. Maalmi, A. El Ouaazizi, R. Benslimane, L. F. C. Lew Yan Voon, A. Diou, and P. Gorria, "Detecting parabolas in ultrasound B-scan images with genetic-based inverse voting Hough transform," in *Proc. IEEE Int. Conf. Acoust., Speech, Signal Process.*, May 2002, vol. 4, pp. IV-3337–IV-3340.

[37] K. S. Park, W. J. Yi, and J. S. Paick, "Segmentation of sperms using the strategic Hough transform," *Ann. Biomed. Eng.*, vol. 25, no. 2, pp. 294–302, Mar./Apr. 1997.

[38] R. M. Rangayyan, *Biomedical Image Analysis*. Boca Raton, FL: CRC Press, 2005.

[39] J. Sklansky, "On the Hough technique for curve detection," *IEEE Trans. Comput.*, vol. C-27, no. 10, pp. 923–926, Oct. 1978.

[40] H. W. Larsen, *The Ocular Fundus: A Color Atlas*. Copenhagen, Denmark: Munksgaard, 1976.

[41] M. Lalonde, M. Beaulieu, and L. Gagnon, "Fast and robust optic disc detection using pyramidal decomposition and Hausdorff-based template matching," *IEEE Trans. Med. Imag.*, vol. 20, no. 11, pp. 1193–1200, Nov. 2001.

[42] Wolfram MathWorld: Parabola. [Online]. Available: http://mathworld.wolfram.com/Parabola.html

[43] J. Xu, O. Chutatape, and P. Chew, "Automated optic disk boundary detection by modified active contour model," *IEEE Trans. Biomed. Eng.*, vol. 54, no. 3, pp. 473–482, Mar. 2007.

[44] C. A. Rogers, *Hausdorff Measures*. Cambridge, U.K.: Cambridge Univ. Press, 1970.

[45] H. Narasimha-Iyer, J. M. Beach, B. Khoobehi, and B. Roysam, "Automatic identification of retinal arteries and veins from dual-wavelength images using structural and functional features," *IEEE Trans. Biomed. Eng.*, vol. 54, no. 8, pp. 1427–1435, Aug. 2007.

[46] E. Grisan and A. Ruggeri, "A divide et impera strategy for automatic classification of retinal vessels into arteries and veins," in *Proc. 25th Annu. Int. Conf. IEEE Eng. Med. Biol. Soc.*, Sep. 2003, vol. 1, pp. 890–893.

[47] I. Kalliomäki and J. Lampinen, "On steerability of Gabor-type filters for feature detection," *Pattern Recognit. Letters*, vol. 28, no. 8, pp. 904–911, Jun. 2007.

[48] M. F. Chiang, P. J. Thyparampil, and D. Rabinowitz, "Interexpert agreement in the identification of macular location in infants at risk for retinopathy of prematurity," *Arch. Ophthalmol.*, vol. 128, no. 9, pp. 1153–1159, Sep. 2010.

[49] C. Heneghan, J. Flynn, M. O'Keefe, and M. Cahill, "Characterization of changes in blood vessels width and tortuosity in retinopathy of prematurity using image analysis," *Med. Image Anal.*, vol. 6, no. 4, pp. 407–429, Dec. 2002.

[50] C. Swanson, K. D. Cocker, K. H. Parker, M. J. Moseley, and A. R. Fielder, "Semiautomated computer analysis of vessel growth in preterm infants without and with ROP," *Brit. J. Ophthalmol.*, vol. 87, no. 12, pp. 1474–1477, Dec. 2003.

[51] P. L. Hildebrand, A. L. Ells, and A. D. Ingram, "The impact of telemedicine integration on resource use in the evaluation ROP . . . analysis of the telemedicine for ROP in Calgary (TROPIC) database," *Invest. Ophthalmol. Vis. Sci.*, vol. 50, p. 3151, 2009, E-Abstract.

Faraz Oloumi (S'05) received the B.Sc. and M.Sc. degrees in electrical and computer engineering from the University of Calgary, Calgary, AB, Canada, in 2009 and 2011, respectively, where he is currently working toward the Ph.D. degree, conducting his research on image processing techniques to extract diagnostic information in fundus images of the retina.

His current interests are biomedical image processing, computer-aided diagnosis, artificial intelligence, pattern analysis, and graphical user interface design.
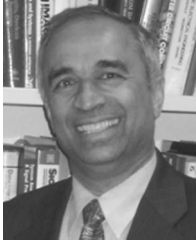
Rangaraj M. Rangayyan (S'77–M'81–SM'83–F'01) received the B.E. degree in electronics and communication from the People's Education Society College of Engineering, University of Mysore, Mandya, India, in 1976 and the Ph.D. degree in electrical engineering from the Indian Institute of Science, Bangalore, India, in 1980.

He is currently a Professor with the Department of Electrical and Computer Engineering, Schulich School of Engineering, University of Calgary, Calgary, AB, Canada, where he is also an Adjunct Professor of surgery and radiology. His research productivity was recognized by an appointment as a "University Professor" at the University of Calgary in 2003. He is the author of two textbooks: *Biomedical Signal Analysis* (IEEE/Wiley, 2002) and *Biomedical Image Analysis* (CRC, 2005). He has coauthored and coedited several other books, including *Color Image Processing With Biomedical Applications* (SPIE, 2011) and three on imaging and image processing for the detection of breast cancer. He has published more than 140 papers in journals and 230 papers in proceedings of conferences. His research interests are in the areas of digital signal and image processing, biomedical signal analysis, biomedical image analysis, and computer-aided diagnosis.

Dr. Rangayyan was elected fellow of The Engineering Institute of Canada in 2002, fellow of the American Institute for Medical and Biological Engineering in 2003, fellow of the International Society for Optical Engineering (SPIE) in 2003, fellow of the Society for Imaging Informatics in Medicine in 2007, fellow of The Canadian Medical and Biological Engineering Society in 2007, and fellow of the Canadian Academy of Engineering in 2009. He was the recipient of the 1997 and 2001 Research Excellence Awards from the Department of Electrical and Computer Engineering, Faculty of Engineering, University of Calgary, and the 1997 Research Award from the Faculty of Engineering, University of Calgary, for his research productivity. He was also a recipient of the Killam Resident Fellowship thrice (1998, 2002, and 2007) in support of his book-writing projects. He was also the recipient of the IEEE Third Millennium Medal in 2000.

Anna L. Ells received the B.Sc. degree from Queen's University, Kingston, Ontario, Canada, in 1983, and the Doctorate in Medicine (*cum laude*) from the University of Ottawa, Ottawa, ON, Canada, in 1987.

She is an Ophthalmologist with the Division of Ophthalmology, Department of Surgery, Alberta Children's Hospital, Calgary, AB, Canada, with dual fellowships in pediatric ophthalmology and medical retina. She has a combined academic hospital-based and private practice. Her research focuses on retinopathy of prematurity (ROP), global prevention of blindness in children, and telemedicine approaches to ROP. She has international expertise and has published extensively in peer-reviewed journals.